JACS
JOURNAL OF THE AMERICAN CHEMICAL SOCIETY
Article
pubs.acs.org/JACS

Disclosure of Key Stereoelectronic Factors for Efficient H_2 Binding and Cleavage in the Active Site of [NiFe]-Hydrogenases

Maurizio Bruschi,*[,†] Matteo Tiberti,[‡] Alessandro Guerra,[‡] and Luca De Gioia*[,‡]

[†]Department of Earth and Environmental Sciences, University of Milano-Bicocca, Piazza della Scienza 1, 20126-Milan, Italy
[‡]Department of Biotechnology and Biosciences, University of Milano-Bicocca, Piazza della Scienza 2, 20126-Milan, Italy

Supporting Information

ABSTRACT: A comparative analysis of a series of DFT models of [NiFe]-hydrogenases, ranging from minimal NiFe clusters to very large systems including both the first and second coordination sphere of the bimetallic cofactor, was carried out with the aim of unraveling which stereoelectronic properties of the active site of [NiFe]-hydrogenases are crucial for efficient H_2 binding and cleavage. H_2 binding to the Ni-SI_a redox state is energetically favored (by 4.0 kcal mol^{-1}) only when H_2 binds to Ni, the NiFe metal cluster is in a low spin state, and the Ni cysteine ligands have a peculiar seesaw coordination geometry, which in the enzyme is stabilized by the protein environment. The influence of the Ni coordination geometry on the H_2 binding affinity was then quantitatively evaluated and rationalized analyzing frontier molecular orbitals and populations. Several plausible reaction pathways leading to H_2 cleavage were also studied. It turned out that a two-step pathway, where H_2 cleavage takes place on the Ni-SI_a redox state of the enzyme, is characterized by very low reaction barriers and favorable reaction energies. More importantly, the seesaw coordination geometry of Ni was found to be a key feature for facile H_2 cleavage. The discovery of the crucial influence of the Ni coordination geometry on H_2 binding and activation in the active site of [NiFe]-hydrogenases could be exploited in the design of novel biomimetic synthetic catalysts.

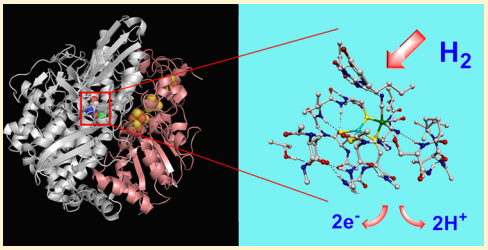

INTRODUCTION

H_2 plays a central role in many chemical processes, and it has promising potential as an environmentally friendly energy carrier. However, a key requirement for the realization of large-scale and sustainable processes, in which H_2 is used for energy storage and delivery, is the development of new catalysts based on inexpensive metals.[1]

Hydrogenases are enzymes involved in the metabolism of H_2 and can be classified, according to the composition of their active site, into three families: [NiFe]-, [FeFe]-, and [Fe]-hydrogenases.[2,3] [NiFe]- and [FeFe]-hydrogenases are classical hydrogenases and catalyze the reversible oxidation of H_2.[4,5] Since in vivo [NiFe]-hydrogenases are generally involved in H_2 oxidation whereas most [FeFe]-hydrogenases are involved in H_2 production, the former are very promising targets for reverse engineering studies aimed at disclosing the stereoelectronic features needed for efficient H_2 binding and cleavage, and therefore drive the design of bioinspired catalysts.[6−8]

In the active site of [NiFe]-hydrogenases, the Ni atom is coordinated by four cysteine residues: two in a terminal fashion and two bridged between the Ni and Fe atoms. The Fe atom is also coordinated by three non-proteic ligands, identified by FTIR and X-ray studies as two CN^- and one CO. A third ligand bridges the two metal atoms in several enzyme forms: an oxygen-containing ligand in oxidized inactive forms and a hydride in reduced active forms.[9−16] Therefore, the coordination environment of Fe and Ni in these enzyme forms can be described as octahedral and distorted trigonal bipyramidal, respectively.

The characterization of several forms of [NiFe]-hydrogenases, differing for their redox and/or protonation state, allowed also to outline key features of the enzyme reactivity (Scheme 1).[16−18]

Scheme 1. Activation Mechanism and Catalytic Cycle of [NiFe]-Hydrogenase[a]

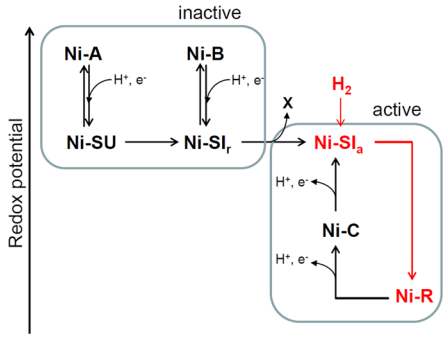

[a]X is an oxygen containing species (probably H_2O) which leaves the active site in the activation process. The part of the catalytic cycle explicitly investigated in this work is shown in red.

Received: August 16, 2013
Published: January 6, 2014

dx.doi.org/10.1021/ja408511y | J. Am. Chem. Soc. 2014, 136, 1803−1814

Scheme 2. Coordination Geometry of Ni^{II} in the NiFe Cluster[a]

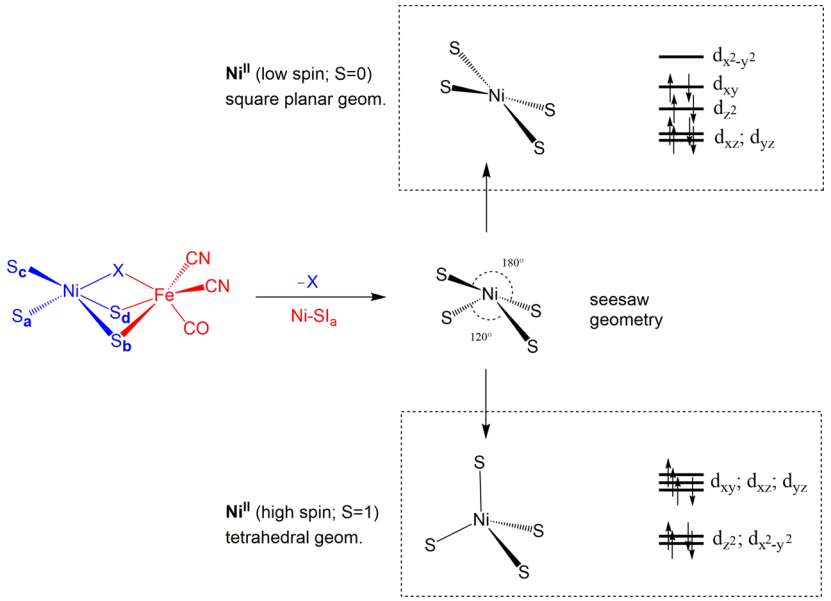

[a]Removal of the bridging ligand X might leave the Ni^{II} ion in a seesaw geometry, which differs from the classical square planar or tetrahedral geometries expected for low or high spin Ni^{II} complexes, respectively.

The oxidized states of [NiFe]-hydrogenases are catalytically inactive and generally referred to as Ni-A and Ni-B. One-electron reduction of the Ni-A and Ni-B forms yields EPR-silent species referred to as Ni-SU and Ni-SI_r, respectively. Protonation of Ni-SI_r and subsequent dissociation of the oxygen containing ligand from the active site yields the Ni-SI_a, form, which has been suggested to correspond to the redox species that binds and activates H_2. In Ni-SI_a, both the Ni and Fe atoms have the formal $Ni^{II}Fe^{II}$ oxidation state, and are four- and five-coordinated, respectively; i.e., the metal ions are both characterized by one vacant coordination position, where H_2 might bind.

Reduction and protonation of the Ni-SI_a form yields a catalytically active paramagnetic form, usually referred to as Ni-C, which corresponds to a $Ni^{III}Fe^{II}$ species characterized by a hydride ligand bridging the two metal ions. One electron reduction of Ni-C leads to the most reduced active form of the enzyme, which is usually referred to as Ni-R. Experimental and computational results converge in the description of the Ni-R form as a species featuring a hydride ligand simultaneously coordinated to Ni^{II} and Fe^{II}. In addition, three distinct forms of Ni-R (Ni-R1, Ni-R2, Ni-R3), which differ for the protonation state, have been identified by IR spectroscopy and theoretical calculations.[19−21]

Even if several [NiFe]-hydrogenase redox forms have been characterized (Scheme 1), some key details about the reactivity of the enzyme are still fuzzy. One ambiguity is related to the spin state and coordination geometry of Ni^{II} in the Ni-SI_a state of the enzyme. In general, when considering sterically unstrained species, four-coordinated low spin Ni^{II} (S = 0) complexes are expected to be characterized by square planar geometry, whereas high spin Ni^{II} (S = 1) species should have tetrahedral geometry. In fact, in most crystallographic structures of [NiFe]-hydrogenases, the Ni atom is five-coordinated, due to the presence of a non-amino-acidic bridging ligand (referred to as X in Scheme 2), and features distorted trigonal bipyramidal geometry. Removal of the exogenous bridging ligand, as occurs when the Ni-SI_a state of the enzyme is formed, might leave the Ni^{II} atom in a peculiar seesaw coordination geometry, if the protein backbone does not allow relaxation of the Ni ligands (Scheme 2).

Another ambiguity is related to the site of H_2 binding. In fact, a species in which H_2 is coordinated to the enzyme active site, but not yet cleaved, is expected to be very short-lived and has not yet been characterized experimentally. Initial DFT calculations carried out using simple models of the $Ni^{II}Fe^{II}$ Ni-SI_a form of the active site showed that H_2 can be weakly bound to the five-coordinated Fe^{II} atom, whereas the corresponding adduct between the Ni^{II} ion and H_2 is unstable.[22] However, this observation was difficult to reconcile with the experimental observation that the gas channel connecting the enzyme surface with the active site ends in front of the Ni atom.[23] Notably, more recent DFT results, obtained using computational models of the active site in which the positions of the four cysteine residues forming the Ni coordination environment were constrained to the corresponding positions observed in the X-ray structure of the enzyme, indicated that both Ni−H_2 and Fe−H_2 adducts correspond to plausible intermediate species in the catalytic mechanism.[24]

According to experimental and computational results, H_2 cleavage should eventually lead to the formation of a species in which one hydrogen atom ends up as a bridging hydride and the other as a proton bound to a terminal cysteine. However, the redox state of the Ni ion when H_2 cleavage takes place is still controversial. In fact, also in this case, computational results depend to some extent on the chemical models adopted in the calculations: H_2 cleavage is predicted to be more likely on a $Ni^{III}Fe^{II}$ species when small models of the NiFe cofactor are considered, whereas calculations carried out using larger models (i.e., including the effect of the environment of the NiFe cofactor) suggest that H_2 cleavage can already take place at the $Ni^{II}Fe^{II}$ redox state.[17,22,24−26] Previous computational studies explored also a scenario where H_2 could bind and be cleaved on an active site form in which a hydride ligand is already bridged

dx.doi.org/10.1021/ja408511y | J. Am. Chem. Soc. 2014, 136, 1803−1814

between the two metal ions.[27] As far as Ni^{II} is assumed for H_2 cleavage, parallel mode EPR,[28] saturation magnetization,[29] and UV−visible MCD[30] investigations suggest a low spin Ni^{II}, whereas L-edge X-ray absorption spectroscopy[31] suggests a high spin Ni^{II}. In this respect, calculation of relative stabilities by DFT can be of little aid due to its known inherent limitations in predicting the correct ground state among different spin states.[32,33]

With the aim of contributing to shed more light on the reactivity of [NiFe]-hydrogenase and, more specifically, disclose which stereoelectronic properties of their active site are crucial for efficient H_2 binding and cleavage, we have adopted a comparative approach, using DFT to study a series of systems ranging from minimal models of the active site, to very large models in which all the aminoacids forming the first and second coordination sphere of the NiFe cluster have been explicitly included. The paper is outlined as follows: In the first section, we present results obtained studying the interaction of H_2 with the Ni-SI_a redox form of the enzyme, with the aim of characterizing the H_2 binding site in [NiFe]-hydrogenases. In the second section, results obtained investigating several plausible reaction pathways leading to H_2 cleavage, considering both heterolytic cleavage and oxidative addition, are presented and compared. In the final section, the stereoelectronic properties of the active site of [NiFe]-hydrogenases that are crucial for efficient H_2 binding and cleavage are discussed in the context of the rational design of novel bioinspired catalysts for H_2 oxidation.

METHODS

Computational Models of the [NiFe]-Hydrogenases. The starting structure for the DFT calculations was based on the X-ray geometry of the *Allochromatium vinosum* (pdb code: 3MYR) [NiFe]-hydrogenase,[34] in which the oxo ligand bridging the Ni and Fe ions was removed, in order to obtain the Ni-SI_a coordination environment, where Ni and Fe are four- and five-coordinated, respectively. In the following, the residues are numbered according to the 3MYR structure (all residues included in the models belong to the large chain of the enzyme, with the exception of Thr17 which belongs to the small chain and, for the sake of clarity, is labeled as Thr17(S)).

Three models of different size have been considered to investigate the effect of the protein environment on the stereoelectronic properties of the active site of [NiFe]-hydrogenases. The validity of such an approach (cluster models) for the DFT investigation of transition metal containing enzymes has been extensively discussed.[35−37]

The largest model, which is schematically shown in Figure 1, contains up to 290 atoms and has a size of about 18 Å. This model includes in its core the bimetallic NiFe cluster, with two CN^- and one CO ligands coordinated to the Fe atom, two cysteine residues terminally coordinated to Ni, and two further cysteine residues bridging the two metal atoms. In the enzyme, two pairs of terminal and bridging cysteine residues (Cys61/Cys64 and Cys555/558) belong to two different Ni binding motifs located at the N- and C-termini of the large subunit. In each binding motif, the cysteine residues are separated by two other residues, which are also contained in the model, so that the pairs Cys61/Cys64 and Cys555/558 are covalently linked together, forming two peptide chains composed by four residues. For the peptide chain Cys555-Ile556-Ala557-Cys558, only the backbone atoms of Ile556 and Ala557 are included in the model, since their side chains are oriented far from the active site, whereas for the peptide chain Cys61-Gly62-Val63-Cys64 the side chain of Val63 is included in the model, since it is close to the vacant coordination site on Ni. These two peptide chains are terminated by selected backbone atoms of residues Ile60, Thr65, Pro554, and Ala559. The second coordination sphere of the NiFe cluster includes the side chains of

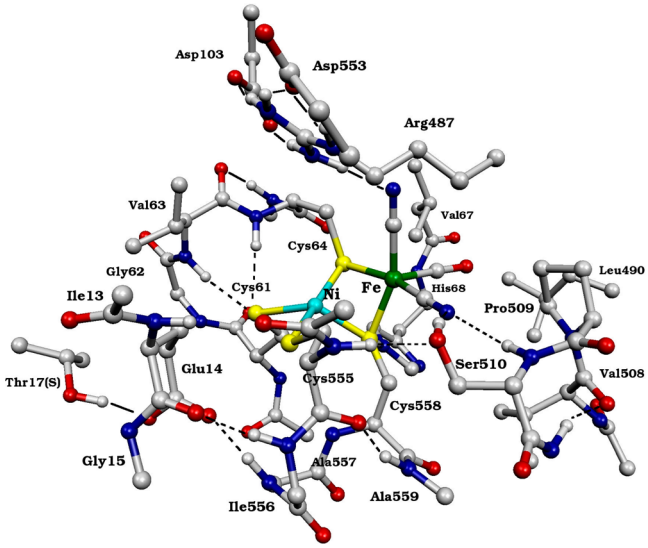

Figure 1. Schematic representation of the largest DFT model of the active site used in this work, derived from the X-ray crystal structure of the [NiFe]-hydrogenase from *Allocromatium vinosum* (pdb code 3MYR).

residues Thr17(S), Asp103, Leu490, Arg487, and Asp553, terminated at the Cα atoms; a peptide chain containing the residues His68 and Val67; a peptide chain containing the carbonyl and the Cα atoms of Val507, and the entire residues Val508, Pro509, and Ser510; and finally a peptide chain containing the carbonyl and Cα atoms of Ile13, the entire residue Glu14, and the N and Cα atoms of Gly15. The truncated residues were saturated with hydrogens. A detailed list of the atoms composing the model is reported in the Supporting Information (Table S1). During geometry optimizations, selected atoms have been constrained to the crystallographic positions, in order to avoid unrealistic distortions at the boundary of the model. These atoms are also indicated in Table S1 (Supporting Information).

Arg487, Asp553, and Asp103 have been included in the model, since they form a network of H-bonds which also involves one CN^- ligand, whereas Ser510 is H-bonded to the other CN^- ligand through its hydroxyl and amide hydrogens. Val67, Leu490, Val508, and Pro509 have been selected because they form a hydrophobic pocket surrounding the $Fe(CN)_2(CO)$ group.

His68 is close to the bimetallic cluster, and when protonated at the εN atom, it can form a H-bond with the sulfur atom of the bridging Cys558. Three protonation states are possible for this residue depending on whether δN, εN, or both atoms are protonated. These protonation states have been investigated in detail by Neese et al.,[38] using a model based on the X-ray structure of the *Desulfovibrio vulgaris Miyazaki F* [NiFe]-hydrogenase; it was concluded that the best comparison between experimental and theoretical data is obtained when His68 is protonated at the εN atom. On the basis of these results, His68 was always modeled as protonated at the εN atom.

The carboxyl group of Glu14 is close to the sulfur atom of Cys555, and it was proposed to be involved in proton transfer from/to the bimetallic cluster.[39−41] In the X-ray structure of the enzyme from *Allochromatium vinosum*, it forms H-bonds with Ala557 and Thr17(S), which were also retained in the model. When investigating H_2 binding to the active site, Glu14 has been modeled both as glutamate and glutamic acid. In the latter case, the proton forms a H-bond with Cys555. Selected backbone atoms of the adjacent residues Ile13 and Gly15 were also added to the model, since they form H-bonds with residues Pro554 and Ile556 belonging to the Cys555/Cys558 binding motif.

A sequence alignment of the large chain of several [NiFe]-hydrogenases, reported in Figure S1 (Supporting Information), shows that residues for which the side chain is included in the model are conserved, emphasizing the possible relevance of these residues in the

dx.doi.org/10.1021/ja408511y | J. Am. Chem. Soc. 2014, 136, 1803−1814

catalytic mechanism of the enzyme. Only backbone atoms of non-conserved residues are included in the model, generally to terminate peptide chains. Exceptions are Val67 and Ser510. The former is replaced by Thr, Ser, Cys, or Ala residues in other [NiFe]-hydrogenases, whereas the latter can be replaced by a Thr residue. A mutagenesis study carried out on the Cys residue replacing Val67 in the [NiFe]-hydrogenase from *Ralstonia eutropha* showed that the effect of the amino-acid substitution on the activity of the enzyme is rather small.[42,43]

The medium-size model contains up to 122 atoms. This model has been used for optimizations of both minimum energy structures and transition states along the H_2 cleavage pathways. The model contains the first coordination sphere of the NiFe cluster, with the cysteine residues terminated at Cα atoms. In the second coordination sphere, the model includes the side chains of Asp103, Asp553, His68, and Thr17(S) terminated at Cβ atoms; the side chain of Glu14 terminated at the Cγ atom; and the side chain of Arg487 terminated at the Cδ atom. The model also contains the side chain of Ser510 and the backbone atoms of Ile556 and Ala557, which are involved in a H-bond network with Glu14. A detailed list of the atoms constituting the medium-size model is given in the Supporting Information (Table S2). For the medium-size model, initial coordinates were taken from the corresponding optimized structure of the large-size model. During geometry optimizations, terminal atoms were constrained to their initial positions (see Table S2, Supporting Information).

A minimal model including only the ligands of the first coordination sphere of the two metal atoms, with formula $[(CH_3S)_4Ni^{II}Fe^{II}(CN)_2(CO)]^{2-}$, has also been considered. In this model, the four cysteine residues are terminated at the Cβ atoms and they are therefore modeled as methylthiolates.

DFT Calculations. Quantum mechanics (QM) calculations have been carried out in the DFT framework with the TURBOMOLE 6.4 suite of programs[44] by using the BP86 functional[45,46] in conjunction with the resolution-of-the-identity (RI) technique.[47] In the large- and medium-size models, an all-electron valence triple-ζ basis set with polarization functions TZVP[48] has been used for Ni, Fe, the atoms of the first coordination sphere, and the residue Glu14. For all other atoms, the double-ζ basis set SV(P)[49] has been used (for details, see the Supporting Information). In the minimal model, the TZVP basis set is used for all atoms.

The effects of the protein environment surrounding the models have been modeled according to the conductor-like screening model (COSMO)[50,51] by considering a polarizable continuum medium with $\varepsilon = 4$. In the case of the large model, geometry optimizations have been carried out in the polarizable continuum medium, whereas for the medium-size model only single point calculations in the polarizable continuum medium have been performed on the geometries optimized in a *vacuum*. It is interesting to note that energy differences calculated in a *vacuum* and in the polarizable continuum medium are very similar, indicating that the size of the models is large enough to be insensitive to nonspecific polarizing effects of the protein environment. The work mainly focuses on H_2 binding and cleavage on the putative $Ni^{II}Fe^{II}$ Ni-SI_a form of the enzyme. Both singlet ($S = 0$) and triplet ($S = 1$) spin states for the Ni atom have been considered. For comparative purposes with previous proposed mechanisms, H_2 binding and cleavage have also been investigated on the $Ni^{I}Fe^{II}$ ($S = 1/2$) and low spin $Ni^{III}Fe^{II}$ ($S = 1/2$) redox states of the active site.

Geometry optimizations of the species along the $Ni^{II}Fe^{II}$ pathways have been performed by including the dispersion interactions correction given by the DFT-D3 Grimme scheme[52−54] on the large model, as implemented in TURBOMOLE,[55] and in order to verify the consistency of results, we have also carried out calculations for the energetically most favored pathways using the M06L functional and the TZVP-SV(P) basis set, on the medium-size model (see the Supporting Information).[56] Calculations with the M06L functional have been performed using the Gaussian 09 program.[57] The results obtained by both including the dispersion interactions correction and using the M06L functional are consistent with those obtained by using the BP86-COSMO scheme and, for the sake of clarity, will be not further commented on in the text (see Tables S5 and S9 in the Supporting Information for the comparison among the energy differences calculated using the different schemes).

Vibrational analysis has been carried out for all species optimized using the medium-size model. Due to the atoms constrained at the original positions, several very small negative eigenvalues of the Hessian were computed. These eigenvalues correspond to torsional vibrational modes involving the constrained atoms.

Transition state search has been performed according to a pseudo Newton−Raphson procedure. First, a geometry optimization of a transition state guess geometry, in which selected internal coordinates are constrained, was performed. The Hessian of such an optimized geometry was then computed, and if one negative eigenvector corresponding to the reaction coordinate was found, the geometry was used as the starting point for the successive optimization steps appliying the trust-region image minimization method,[58] which is designed to maximize the energy along one of the eigenvectors (i.e., the chemically relevant one), while minimizing it in all other directions. As discussed above, the presence of constrained atoms resulted in the occurrence of several imaginary frequencies. However, the eigenvector corresponding to the reaction coordinate was easily identified as the one with an eigenvalue much lower than the other negative eigenvalues.

Energy profiles as a function of the S_a−Ni−S_b angle (see Scheme 2 for atom labeling) have been calculated for the small model $[(CH_3S)_4Ni^{II}Fe^{II}(CN)_2(CO)]^{2-}$, which includes only the ligands of the first coordination sphere ($^1\mathbf{2_S}$). The model labeled $^1\mathbf{2_S}$**-P** results from a constrained geometry optimization of $^1\mathbf{2_S}$, in which all atoms with the exception of hydrogens have been fixed at the position computed for the large model (see the Results and Discussion for model labeling). It should be noted that full geometry optimization of $^1\mathbf{2_S}$ does not lead to the absolute minimum, because rotation of the CH_3 groups leads to a conformation lower in energy by 1.1 kcal mol^{-1}. However, we will consider $^1\mathbf{2_S}$ as the reference geometry for the square planar form, since it provides the smallest reorganization of the pendant groups when moving from $^1\mathbf{2_S}$**-P** to $^1\mathbf{2_S}$. Geometry optimizations of $^1\mathbf{2_S}$ have also been carried out constraining the S_a−Ni−S_b angle at selected values from 160 to 100°. The same protocol has been applied to the H_2-bounded form of $^1\mathbf{2_S}$ ($^1\mathbf{2_S}$**-Ni$_{H_2}$**). The H_2 binding energy as a function of the S_a−Ni−S_b angle was then calculated as the energy difference between products and reactants for the reaction

$$^1\mathbf{2_S} + H_2 \rightarrow {}^1\mathbf{2_S}\text{-}\mathbf{Ni_{H_2}}$$

in which $^1\mathbf{2_S}$ and $^1\mathbf{2_S}$**-Ni$_{H_2}$** feature the same S_a−Ni−S_b angle.

Energy profiles as a function of the S_a−Ni−S_b angle have also been calculated on the mononuclear model $[(CH_3S)_4Ni^{II}]^{2-}$, which includes the Ni ion and its first coordination sphere, using the same procedure described above.

RESULTS AND DISCUSSION

H_2 Binding to the Ni-SI_a Form. Initially, with the aim of characterizing the H_2 binding site in [NiFe]-hydrogenases, we have studied the interaction of H_2 with the Ni-SI_a redox form of the enzyme. Both low and high spin states have been taken into account.

The computational model used in this investigation has been derived from the crystallographic structure of the [NiFe]-hydrogenase from *Allochromatium vinosum*, which should correspond to the Ni-B form, and therefore features an oxo-containing ligand which bridges the two metal atoms in the active site. The removal of this ligand from the crystallographic structure, to generate models of the Ni-SI_a form, leaves the Ni atom in a distorted seesaw conformation in which the S_a−Ni−S_b and S_c−Ni−S_d angles are 109.2 and 165.8°, respectively (see Scheme 2 for atom labeling).

dx.doi.org/10.1021/ja408511y | J. Am. Chem. Soc. 2014, 136, 1803−1814

Scheme 3. Schematic Representation of the Possible Reaction Pathways for H_2 Binding to the Ni-SI_a Form of the Active Site of [NiFe]-Hydrogenases[a]

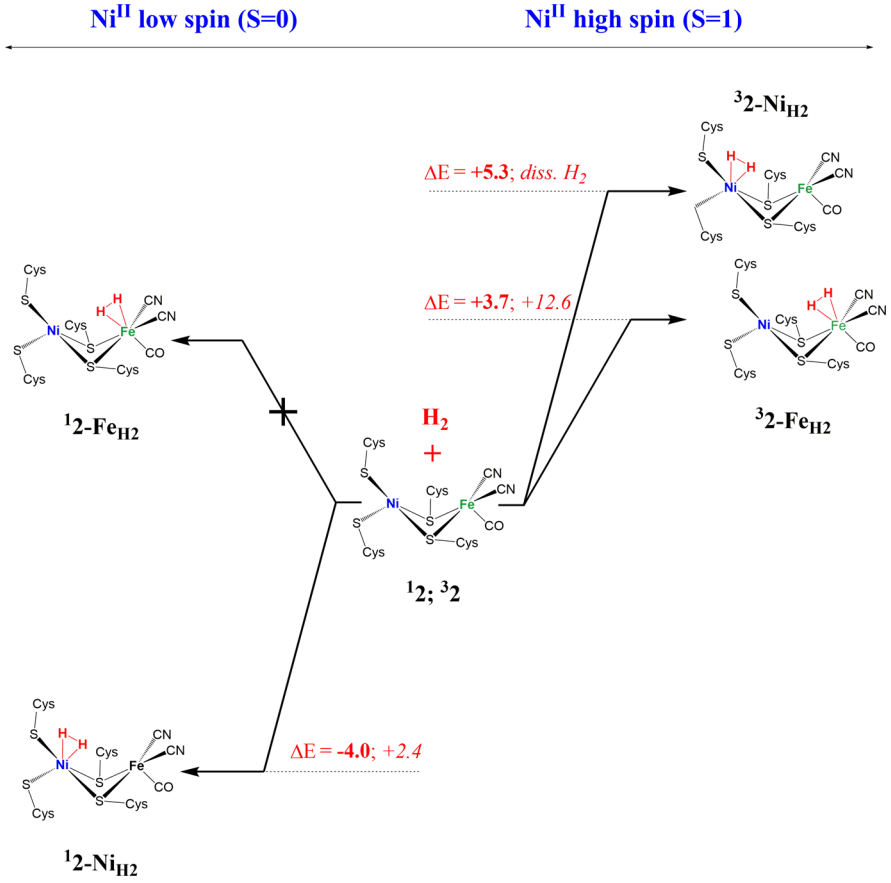

[a]Values in bold refer to calculations performed using the large model, whereas values in italic refer to calculations performed using the medium-size model. Energies are in kcal mol^{-1}.

Throughout the paper, computational models will be labeled according to the general scheme ^{i}**K-X**, where ***i*** = spin state of the complex, ***K*** = formal oxidation state of the Ni ion, and ***X*** = specific chemical nature of the complex. For the sake of clarity, when necessary, the size of the model (**S**, **M**, and **L** for small, medium, and large models, respectively) will be indicated as a subscript after ***K***.

Geometry optimization of a large model of the Ni-SI_a form (see the Methods for details), either in the low or high spin state ($^{1}\mathbf{2}_{L}$ and $^{3}\mathbf{2}_{L}$, respectively), does not lead to a significant structural rearrangement of the Ni coordination sphere relative to the X-ray structure. In particular, the S_a−Ni−S_b and S_c−Ni−S_d angles in the geometry optimized models are 123.9 and 150.7°, respectively, for the low spin Ni^{II} model and 121.9 and 155.5°, respectively, for the high spin Ni^{II} model. In order to check the influence of the constraints imposed to the terminal atoms of the model on the Ni coordination geometry, we also performed geometry optimization after removing all of the constraints on the atoms which are covalently connected to the metal cluster (i.e., all constraints on atoms of the two Ni-binding motifs). However, the geometry of the Ni atom remained essentially identical to the one obtained from the corresponding constrained geometry optimization.

The role of the protein environment in tuning the coordination geometry of Ni in the Ni-SI_a form is highlighted by the analysis of the geometries obtained using a medium-size model (see the Methods for details). In particular, for the low spin species ($^{1}\mathbf{2}_{M}$), the S_a−Ni−S_b angle is significantly larger than in the corresponding large model (S_a−Ni−S_b = 137.8°, S_c−Ni−S_d = 160.4°), indicating that the conformation is approaching the square planar geometry, whereas for the high spin species ($^{3}\mathbf{2}_{M}$) the S_c−Ni−S_d angle decreases considerably (S_a−Ni−S_b = 110.0°, S_c−Ni−S_d = 106.0°), indicating that the conformation is approaching the tetrahedral geometry.

In light of the results obtained with large- and medium-sized models, it can be suggested that the seesaw conformation of the bimetallic cluster in the Ni-SI_a form may be favored by the network of H-bonds occurring nearby the active site. In particular, the Cys555/Cys558 binding motif is included in a small α-helix at the C-terminus of the large subunit, which may be crucial for the coordination geometry of the thiol ligands. In addition, the H-bonds between His68/Cys558, Glu14/Pro554, Ile556/Glu14, and Cys555/Ser510 can impart further rigidity to the structure of the active site.

The computed energy difference between the low and high spin forms of Ni-SI_a, calculated using the large model, is 6.7 kcal mol^{-1} in favor of the former. However, due to the known inherent limitations of DFT in predicting the correct ground state among different spin states,[32,33] we cannot consider this value as reliable for the correct assignment of the spin state of the Ni-SI_a form. More relevantly for the aim of our study, binding of H_2 to the low spin Ni^{II} atom in $^{1}\mathbf{2}_{L}$ is favorable (−4.0 kcal mol^{-1}; $^{1}\mathbf{2}_{L}$-$\mathbf{Ni}_{H_2}$; see Scheme 3), whereas the corresponding adduct in which H_2 binds to the Fe^{II} ion is

dx.doi.org/10.1021/ja408511y | J. Am. Chem. Soc. 2014, 136, 1803−1814

unstable, resulting in H_2 release from Fe and binding to Ni during geometry optimization. As for the high spin $Ni^{II}Fe^{II}$ Ni-SI_a model, H_2 can bind to both Ni and Fe ions, but in both cases, the reaction is endoenergetic by 5.3 and 3.7 kcal mol^{-1}, respectively ($^3\mathbf{2_L}$-$\mathbf{Ni_{H_2}}$ and $^3\mathbf{2_L}$-$\mathbf{Fe_{H_2}}$ in Scheme 3). Therefore, the metal atom featuring the highest affinity for H_2 is the Ni ion in the low spin $Ni^{II}Fe^{II}$ redox state of the enzyme. $^1\mathbf{2_L}$-$\mathbf{Ni_{H_2}}$ is characterized by a distorted trigonal bipyramidal geometry, with the S_a–Ni–S_b and S_c–Ni–S_d angles equal to 110.3 and 174.5°, respectively, and with the H_2 atoms at 1.63 and 1.64 Å from the Ni ion.

The investigation of H_2 binding using medium-size models highlights again the noninnocent role of the protein environment. In fact, binding of H_2 to the low spin Ni^{II} atom in the medium-size model ($^1\mathbf{2_M}$-$\mathbf{Ni_{H_2}}$) is endoenergetic by 2.4 kcal mol^{-1}. In addition, H_2 does not bind to Ni in the high spin species, whereas it can still bind to Fe ($^3\mathbf{2_M}$-$\mathbf{Fe_{H_2}}$) but with a reaction endoenergetic by 12.6 kcal mol^{-1}.

With the aim of revealing which stereoelectronic factors are crucial for the observed regiochemistry of H_2 binding, we have studied also minimal models of the [NiFe]-hydrogenase active site, which include only the first coordination sphere of the metal ions. The unrestrained optimization of the low spin $[(CH_3S)_4Ni^{II}Fe^{II}(CN)_2(CO)]^{2-}$ model ($^1\mathbf{2_S}$) yields a structure which differs from the corresponding optimized structure of the large model $^1\mathbf{2_L}$ mainly for the S_a–Ni–S_b angle (S_a–Ni–S_b and S_c–Ni–S_d = 160.4 and 168.8°, respectively in $^1\mathbf{2_S}$). In other words, the Ni coordination sphere can be described as having a distorted square planar geometry in the small model $^1\mathbf{2_S}$, differently from the distorted seesaw geometry observed in $^1\mathbf{2_L}$ (see Scheme 4).

Scheme 4. Distorted Seesaw Geometry of Ni in the Large Model $^1\mathbf{2_L}$ Corresponding to the Ni-SI_a State of the Enzyme (left) and Distorted Square Planar Geometry in the Small Model $^1\mathbf{2_S}$ (right)[a]

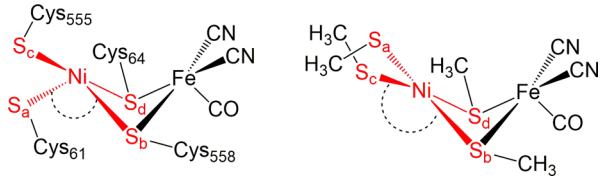

[a]Smooth transition between the two geometries can be obtained varying the angle S_b–Ni–S_a.

H_2 cannot bind to the Ni ion in $^1\mathbf{2_S}$ (the geometry optimization of the H_2 adduct leads to dissociation of H_2), whereas it can bind to the Fe atom (ΔE = −1.9 kcal mol^{-1}). On the other hand, in a $^1\mathbf{2_S}$ model variant (hereafter labeled as $^1\mathbf{2_S}$-**P**) in which all atoms with the exception of hydrogens were constrained to the positions calculated for the large model $^1\mathbf{2_L}$, H_2 can bind the Ni atom (ΔE = −1.2 kcal mol^{-1}), whereas H_2 binding to the Fe atom does not take place. Therefore, the comparison between unconstrained and constrained small models of the [NiFe]-hydrogenase active site clearly highlights that the geometry of the ligands coordinated to the Ni atom is a crucial factor for the regiochemistry of H_2 binding.

To better evaluate the effect of the Ni coordination geometry on the regiochemistry of H_2 binding, we have also studied the energetics of H_2 binding as a function of the S_a–Ni–S_b angle, carrying out a series of geometry optimizations of $^1\mathbf{2_S}$ and the corresponding H_2 adduct ($^1\mathbf{2_S}$-$\mathbf{Ni_{H_2}}$), in which the S_a–Ni–S_b angle was kept fixed at several values in the range 100–160°. It turned out that the Ni–H_2 adduct can be formed only when the S_a–Ni–S_b angle is lower than 135°. As shown in Figure 2,

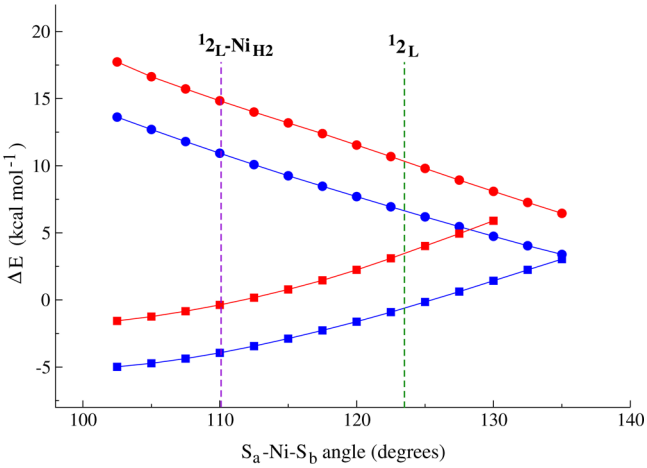

Figure 2. H_2 binding energy to Ni calculated as a function of the S_a–Ni–S_b angle for the complex $^1\mathbf{2_S}$ (blue line with square symbols) and the complex $[(CH_3S)_4Ni]^{2-}$ (red line with square symbols). Energy variation calculated as a function of the S_a–Ni–S_b angle with respect to the optimum geometry for the complex $^1\mathbf{2_S}$ (blue line with circle symbols) and the complex $[(CH_3S)_4Ni]^{2-}$ (red line with circle symbols). Only results in the range 100–135° are reported, because H_2 does not bind to Ni for larger values of the angle. Vertical green and violet dashed lines indicate the values of the S_a–Ni–S_b angle measured in $^1\mathbf{2_L}$ and $^1\mathbf{2_L}$-$\mathbf{Ni_{H_2}}$, respectively.

the corresponding reaction energy varies from about +3 kcal mol^{-1} when the S_a–Ni–S_a angle is 135° to about −5 kcal mol^{-1} when the angle is 102.5°. Correspondingly, the energy of $^1\mathbf{2_S}$ increases with the bending of the S_a–Ni–S_b angle (see Figure 2). In particular, $^1\mathbf{2_S}$-**P** is about 11 kcal mol^{-1} higher in energy than the unconstrained $^1\mathbf{2_S}$ model. Therefore, the data reported in Figure 2 highlight a trade-off between the H_2 binding energy, which becomes more favorable for lower angles, and the destabilization of the cofactor, which increases for lower angles.

Finally, we have also studied H_2 binding to the minimal $[(CH_3S)_4Ni]^{2-}$ model, which is obtained by removing the $Fe(CN)_2(CO)$ moiety from $^1\mathbf{2_S}$, to evaluate how the Fe-$(CN)_2(CO)$ moiety affects H_2 binding. $[(CH_3S)_4Ni]^{2-}$ can bind H_2 only when the S_a–Ni–S_b angle is lower than 130°, and the H_2 binding energy is systematically less favorable by about 3 kcal mol^{-1} than in $^1\mathbf{2_S}$. In addition, as shown in Figure 2, the energy of the $[(CH_3S)_4Ni]^{2-}$ complex as a function of the S_a–Ni–S_b angle increases more steeply than for $^1\mathbf{2_S}$.

To rationalize the effect of the S_a–Ni–S_b angle on the regiochemistry of H_2 binding, we have analyzed the frontier molecular orbitals (FMOs) of $^1\mathbf{2_S}$ (see Figure 3 and Figure S2 in the Supporting Information).

In the unconstrained $^1\mathbf{2_S}$ structure, the LUMO is mainly localized on the Fe atom and features a lobe with an orientation well suited to act as an electron acceptor in H_2 binding (Figure 3), whereas the HOMO can be described as an antibonding combination of the p orbitals of the terminal S atoms and one d orbital of the Ni atom (see Figure S2 in the Supporting Information). When considering the FMOs of $^1\mathbf{2_S}$-**P**, the LUMO is mainly localized on the Ni atom and a lobe is

dx.doi.org/10.1021/ja408511y | J. Am. Chem. Soc. 2014, 136, 1803–1814

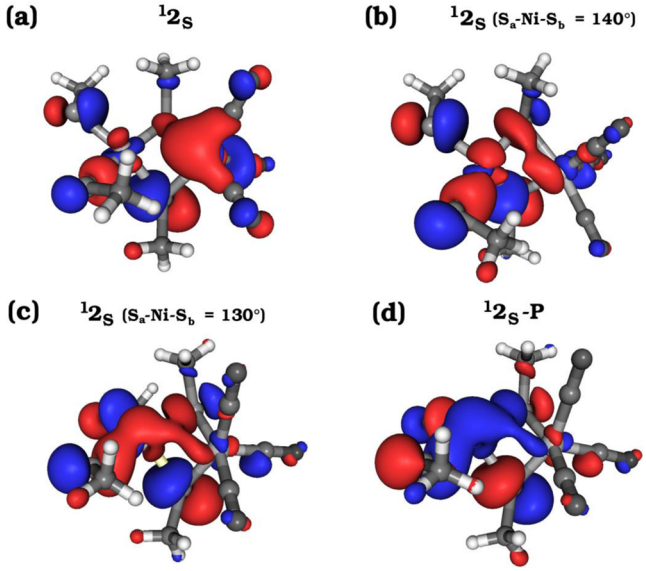

Figure 3. LUMO of ^{1}2$_S$ (a) in the fully unconstrained optimized structure; (b, c) in the structures with the S_a–Ni–S_b angle constrained to 140 and 130°, respectively; and (d) in the model variant ^{1}2$_S$-**P** in which the Ni ligands were constrained to the positions observed in the enzyme.

oriented in the region between the two metal atoms. Inspection of the orbital energies reveals that only the LUMO energy is affected by variation of the S_a–Ni–S_b angle, decreasing when the bending of this angle increases (see Figure S3 in the Supporting Information). The localization of the LUMO on the two different metal atoms in ^{1}2$_S$ and ^{1}2$_S$-**P** may explain why in the fully optimized complex H_2 can bind to the Fe atom but not to the Ni atom, whereas in the complex featuring the geometry observed in the enzyme H_2 can bind to the Ni atom but not to the Fe atom.

The analysis of the electronic properties of Ni-SI$_a$ models suggests that the S_a–Ni–S_b angle is also crucial for tuning the reactivity of H_2. In fact, analysis of the population of the σ and σ^* orbitals of H_2 reveals that the former decreases and the latter increases as a function of the S_a–Ni–S_b angle (see Figure S4 in the Supporting Information), indicating that both donation of electron density from H_2 to Ni and back-donation from Ni to H_2 are affected by the value of this angle. Correspondingly, the H–H bond distance increases as a function of the S_a–Ni–S_b angle. The large increase of the σ^* orbital population suggests that H_2 could be activated through an oxidative addition mechanism.

H$_2$ Cleavage on the Ni-SI$_a$ Form. After the analysis of the factors affecting the H_2 binding step, we have investigated plausible reaction pathways leading to H_2 cleavage. In particular, starting from the lowest energy (i.e., most favored) Ni–H_2 adduct (which corresponds to H_2 binding to the Ni ion in the low spin Ni-SI$_a$ redox state), we have considered two different pathways (Scheme 5): (*A*) heterolytic cleavage of H_2 in which the S atom of Cys555 extracts a proton from H_2, with the concomitant formation of a terminal hydride coordinated to Ni, followed by transfer of the hydride to a bridged position between the two metal atoms; (*B*) oxidative addition of H_2 with the formation of an intermediate featuring one terminal and one bridged H atom, followed by proton transfer from Ni to the S atom of Cys555. We have also considered analogous pathways in which the S atom of Cys61 is involved in the proton abstraction from H_2. However, activation and reaction energies were systematically higher (data not shown), indicating that Cys555 is the residue that is transiently protonated upon H_2 cleavage. The pathways featuring protonation of Cys61 may be less favorable due to the formation of two H-bonds between the sulfur atom of Cys61 and the amide hydrogen atoms of residues Val63 and Cys64, which make the sulfur atom less basic, and provide some steric hindrance for its protonation.

In the following, the atoms of hydrogen which migrate to the S atom of Cys555 (S_c in Scheme 2) and to the NiFe bridging position will be labeled H_b and H_a, respectively. Geometrical parameters discussed in the text will refer to the large model for minimum energy species and to the medium-size model for

Scheme 5. Schematic Representation of the Possible Reaction Pathways for Dihydrogen Activation and Cleavage in the Active Site of [NiFe]-Hydrogenases[a]

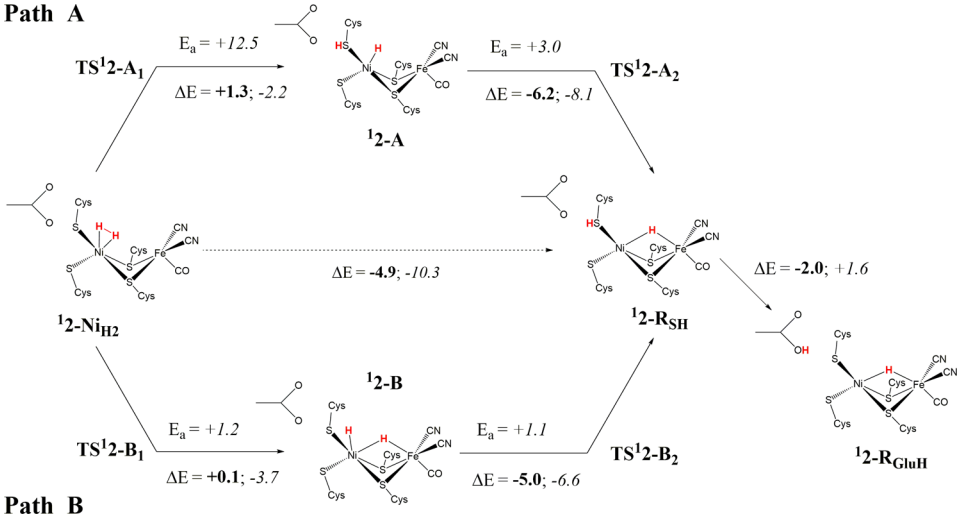

[a]Values in bold refer to calculations performed using the large model, whereas values in italic refer to calculations performed using the medium-size model. Energy differences and activation energies are in kcal mol^{-1}.

dx.doi.org/10.1021/ja408511y | J. Am. Chem. Soc. 2014, 136, 1803–1814

transition states (TS). Comparison of selected geometry parameters of the large- and medium-size models is given in Figure 4.

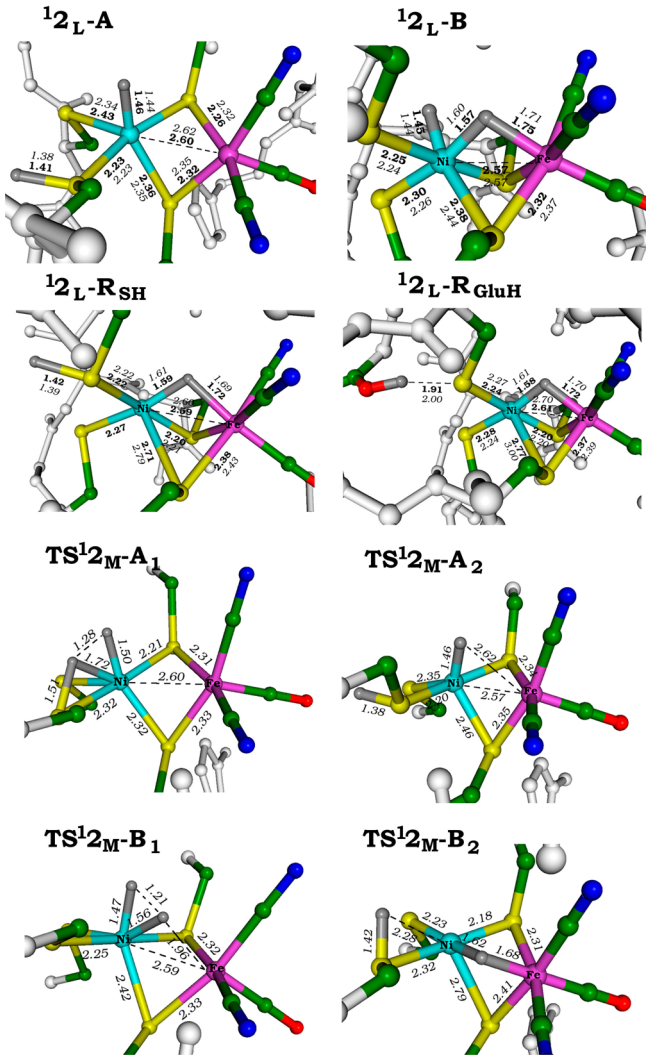

Figure 4. Schematic representation of the optimized structures of the species in pathways *A* and *B* with selected distances in Å. In bold and italic are shown the distances calculated using the large- and medium-size models, respectively. Transition states have been calculated only using the medium-size model, and therefore, only one set of distances is reported. For the sake of clarity, hydrogen atoms, with the exception of H_a and H_b, are not shown.

The first step in pathway *A* transiently yields a terminal hydride species (**^{1}2-A** in Scheme 5 and Figure 4). A similar terminal hydride species was characterized for the more oxidized Ni-C form of the enzyme by Neese et al.,[38] even if it was 22 kcal mol^{-1} less stable than the corresponding μ-hydride form. The activation energy for this step is 12.5 kcal mol^{-1}. In the corresponding transition state (**TS^{1}2-A$_1$** in Scheme 5 and Figure 4), the two atoms of dihydrogen are 1.28 Å apart. The intermediate **^{1}2-A** is almost isoenergetic with the reactant **^{1}2-Ni$_{H_2}$**; the energy difference is +1.3 and −2.2 kcal mol^{-1} for the large- and medium-size models, respectively. In **^{1}2$_L$-A**, the Ni atom features a pseudo square pyramidal coordination, in which the S atom of Cys61 (S_a in Scheme 2) occupies the apical position. The H_a−Ni distance and the H_a−Ni−Fe angle in **^{1}2$_L$-A** are 1.46 Å and 100.3°, respectively. **^{1}2-A** is a transient species that, in the second step of pathway *A*, can quickly rearrange to the μ-hydride species **^{1}2-R$_{SH}$**. The activation energy for this step is as small as 3.0 kcal mol^{-1}, and the reaction is exoenergetic by −6.2 and −8.1 kcal mol^{-1} considering the large- and medium-size models, respectively. The geometry of the transition state (**TS^{1}2-A$_2$** in Scheme 5 and Figure 4) is similar to that of the intermediate, with the H_a−Ni and H_a−Fe distances and the H_a−Ni−Fe angle equal to 1.46 Å, 2.62 Å, and 75.8°, respectively.

The reaction product of the second step (**^{1}2-R$_{SH}$** in Scheme 5 and Figure 4) should correspond to the reduced Ni-R form of the enzyme.[59,60,16] In this species, H_a asymmetrically bridges the two metal atoms (H_a−Ni = 1.59 Å; H_a−Fe = 1.72 Å in **^{1}2$_L$-R$_{SH}$**), whereas H_b is migrated as a proton to the S_c atom. This form is characterized by a significant elongation of the Ni−S_b bond (2.7 Å **^{1}2$_L$-R$_{SH}$**).

Pathway *B* is also characterized by two steps. In the first step, H_2 undergoes a formal oxidative addition, in which H_b remains terminally coordinated to Ni and H_a moves to a bridging position between the two metal atoms, yielding the **^{1}2-B** intermediate (see Scheme 5 and Figure 4). The oxidative addition step in pathway *B* is almost barrierless (activation energy 1.2 kcal mol^{-1}). The intermediate **^{1}2-B** is isoenergetic with the reactant (ΔE = +0.1), or more stable than the reactant by −3.7 kcal mol^{-1}, for the large- and medium-size models, respectively. Also, the second step of pathway *B*, corresponding to the Ni-to-S_c proton migration, is almost barrierless (E_a = 1.1 kcal mol^{-1}), leading to the product **^{1}2$_L$-R$_{SH}$** which is −5.0 or −6.6 kcal mol^{-1} lower in energy than **^{1}2-B** for the large- and medium-size models, respectively.

In the transition state of the first step of path *B* (**TS^{1}2-B$_1$** in Scheme 5 and Figure 4), the H_a atom asymmetrically bridges the Ni and Fe atoms (H_a−Ni = 1.56 Å; H_a−Fe = 1.96 Å), while the H_b atom is moving to a terminal position on Ni (H_b−Ni = 1.47; H_b−Ni−Fe = 91.8°). The H_a−H_b distance and the Ni−Fe bond length are 1.21 and 2.59 Å, respectively. The intermediate **^{1}2$_L$-B** has a pseudo octahedral coordination of the Ni atom, in which the H_b−Ni−H_a angle is 77.2° and the H_a−H_b distance is 1.89 Å. The bridging H_a atom is slightly closer to Ni than Fe (H_a−Ni = 1.57 Å; H_a−Fe = 1.75 Å), while the terminal H_b atom (H_b−Ni = 1.45 Å) is slightly bent in the direction of S_c (H_b−Ni−S_c = 82.9°). The H_b atom moves to an asymmetric bridging position between Ni and S_c in the transition state of the second step of pathway *B* (**TS^{1}2-B$_2$** in Scheme 5 and Figure 4), in which it is much closer to S_c than to Ni (H_b−S_c = 1.42 Å; H_b−Ni = 2.28 Å). The Ni−S_b distance in **TS^{1}2-B$_2$** is 2.79 Å, and is very similar to that observed in the product **^{1}2$_L$-R$_{SH}$**.

As shown in Scheme 5, we have also investigated the proton transfer from the S_c atom of Cys555 in **^{1}2$_L$-R** to the carboxylate group of Glu14 (**^{1}2$_L$-R$_{GluH}$** in Scheme 5 and Figure 4). This process is almost isoenergetic (ΔE = −2.0 and +1.6 kcal mol^{-1} for the large- and medium-size models, respectively), suggesting that **^{1}2-R$_{SH}$** and **^{1}2-R$_{GluH}$** are in equilibrium, and may correspond to two different Ni-R forms characterized by spectroscopic methods, as also recently suggested by Neese et al.[21]

It is interesting to note that, after the monoelectronic oxidation of **^{1}2$_L$-R$_{SH}$** yielding the putative Ni-C form of the enzyme, the species in which Cys555 is protonated does not correspond to an energy minimum, because the proton spontaneously migrates during geometry optimization to the

dx.doi.org/10.1021/ja408511y | J. Am. Chem. Soc. 2014, 136, 1803−1814

carboxylic group of Glu14. In addition, the Ni−S_b bond length significantly shortens to the value of 2.40 Å, in very good agreement with the distance observed in the crystallographic structures of reduced forms of the enzyme (data not shown).[13,61]

Comparison with Other Proposed Mechanisms. Previous theoretical investigations suggested that H_2 binding and/or cleavage can occur on species where the redox state of Ni is more reduced (Ni^I) or more oxidized (Ni^{III}) than Ni^{II}. Therefore, with the aim of obtaining homogeneous and comparable results, we reinvestigated the reaction profiles of these mechanisms using our largest model.

A mechanism involving the Ni^I redox state in H_2 binding and cleavage has been recently proposed.[26] According to this scenario, heterolytic cleavage of H_2 takes place on Ni-SI_a only in the initial step. Then, a Ni^I form of the active site is formed, which was proposed to efficiently bind and cleave H_2 molecules via an oxidative addition step. In order to reinvestigate this mechanism, we started from a Ni^I form (hereafter labeled $^2\mathbf{1}_L$) obtained by one-electron reduction of $^1\mathbf{2}_L$. H_2 can bind to the Ni atom of $^2\mathbf{1}_L$, yielding the H_2 adduct $^2\mathbf{1}_L$-$\mathbf{Ni}_{H_2}$ (see Figure 5),

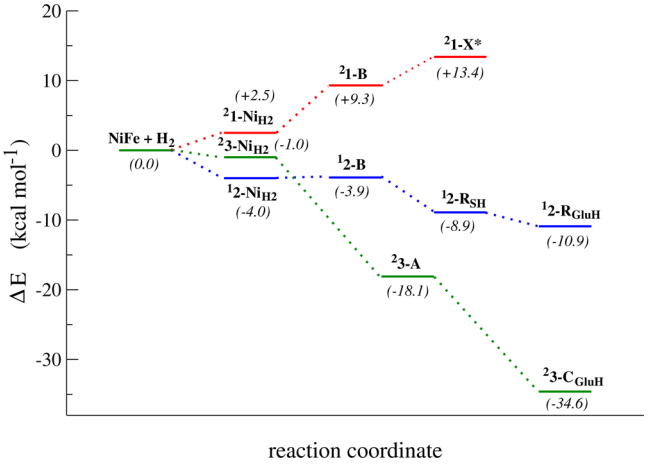

Figure 5. Energy profile of H_2 binding and cleavage along the lowest energy pathway (only minimum energy species are considered) for the low spin Ni^{II} (blue line), Ni^I (red line), and Ni^{III} redox forms of the active site. In parentheses are the relative energies (in kcal mol^{-1}) with respect to **NiFe** + H_2 (**NiFe** = $^2\mathbf{1}$, $^1\mathbf{2}$, or $^2\mathbf{3}$) using the large model.

but the process is endoenergetic by 2.5 kcal mol^{-1}. The corresponding adduct in which H_2 binds to the Fe^{II} ion of $^2\mathbf{1}_L$ is 20.1 kcal mol^{-1} higher in energy than the reactants, and its formation can therefore be ruled out. In $^2\mathbf{1}_L$-$\mathbf{Ni}_{H_2}$, the Ni−H bonds are longer (1.701 and 1.710 Å) than in $^1\mathbf{2}_L$-$\mathbf{Ni}_{H_2}$, and correspondingly, the H_2 molecule is less activated. Oxidative addition of H_2 on the Ni atom of $^2\mathbf{1}_L$-$\mathbf{Ni}_{H_2}$ yields the intermediate $^2\mathbf{1}_L$-**B** (see Figure 5). However, $^2\mathbf{1}_L$-**B** is higher in energy than the H_2 adduct by about 7 kcal mol^{-1}, a value which added to the H_2 binding energy indicates that this reaction pathway is energetically disfavored when compared to H_2 activation and cleavage on a Ni^{II} species. In addition, the step corresponding to the proton transfer from Ni to Cys555 to give $^2\mathbf{1}_L$-**X*** is also endoenergetic by about 4 kcal mol^{-1}. The intermediate in which H_2 is cleaved heterolytically with protonation of Cys555 and concomitant formation of a terminal hydride coordinated to Ni has not been characterized, because the terminal hydride spontaneously moves to the bridging position during geometry optimization. Therefore, the heterolytic cleavage of H_2 on the Ni^I form yields in one step the $^2\mathbf{1}_L$-**X*** species, which is about 11 kcal mol^{-1} higher in energy than $^2\mathbf{1}_L$-$\mathbf{Ni}_{H2}$.

Another scenario was explored by Hall et al., showing that H_2 cleavage on a Ni^{III} form of the active site is more favorable than on the corresponding high and low spin Ni^{II} forms, suggesting that binding of H_2 on Ni^{II} is followed by oxidation to a Ni^{III} H_2 adduct.[62−64] In fact, according to the calculations carried out using our large model, H_2 binding can occur to both Ni^{III} and Fe^{II} ($^2\mathbf{3}_L$-$\mathbf{Ni}_{H_2}$ and $^2\mathbf{3}_L$-$\mathbf{Fe}_{H_2}$), and both H_2 adducts are almost isoenergetic with the reactants (ΔE_{H_2Ni} = −1.0 kcal mol^{-1}; ΔE_{H_2Fe} = −0.1 kcal mol^{-1}). A formal oxidative addition reaction on $^2\mathbf{3}_L$-$\mathbf{Ni}_{H_2}$, to yield an intermediate featuring one terminal and one bridged H atom ($^2\mathbf{3}_L$-**B**), is an endoenergetic process by 2.5 kcal mol^{-1} (see Figure 5). On the other hand, the heterolytic cleavage yielding an intermediate ($^2\mathbf{3}_L$-**A**) featuring one proton on S_c and one hydride terminally coordinated to the Ni atom is strongly exoenergetic (−17.1 kcal mol^{-1}). It should be noted that in $^2\mathbf{3}_L$-**A** the proton initially placed on S_c spontaneously transfers to Glu14 during geometry optimization. Migration of the hydride from the terminal to the bridged position, yielding $^2\mathbf{3}$-$\mathbf{C}_{GluH}$ is also an exoenergetic step by −16.5 kcal mol^{-1}. Therefore, cleavage of H_2 on the Ni^{III} form of the active state is calculated to be an exoenergetic process by about 35 kcal mol^{-1}. The large stabilization of the $^2\mathbf{3}$-$\mathbf{C}_{GluH}$ product when compared to the H_2 adduct may suggest that, indeed, oxidation of Ni^{II} to Ni^{III} and H_2 cleavage might occur through a concerted mechanism. In this respect, a rough estimate of the oxidation propensity of the active site can be obtained analyzing the HOMO energies of the species involved in the reaction mechanism. Figure 6 shows the HOMO energies of the species

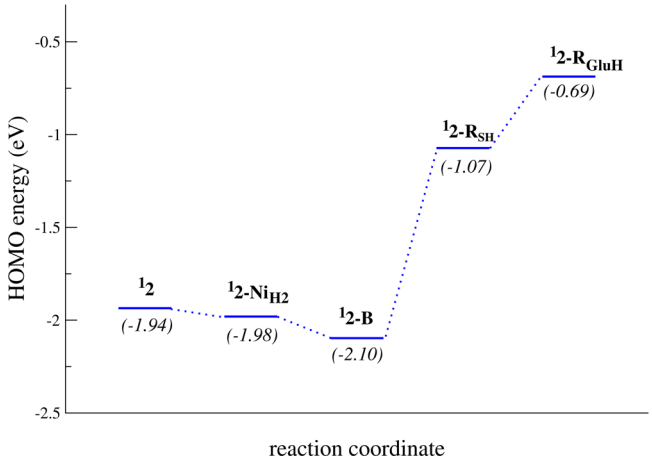

Figure 6. HOMO energies along the lowest energy pathway (only minimum energy species are considered) for the low spin Ni^{II} redox form of the active site. In parentheses are the HOMO energies in eV.

along the lowest energy profile in the cleavage of H_2 on the low spin Ni^{II} form. It is interesting to note that the HOMO energy is nearly constant along the reaction pathway in $^1\mathbf{2}$, $^1\mathbf{2}$-$\mathbf{Ni}_{H_2}$ and $^1\mathbf{2}$-**B**, whereas it increases significantly in the $^1\mathbf{2}$-$\mathbf{R}_{SH}$ product, suggesting that an electron can be easily extracted from the latter form. This observation is in line with the experimental evidence that Ni-SI_a and Ni-R forms in the enzyme are in a non-redox equilibrium.

dx.doi.org/10.1021/ja408511y | J. Am. Chem. Soc. 2014, 136, 1803−1814

Scheme 6. The Most Plausible Catalytic Mechanism for H_2 Oxidation in [NiFe]-Hydrogenases, according to the Computational Results Obtained in the Present Work

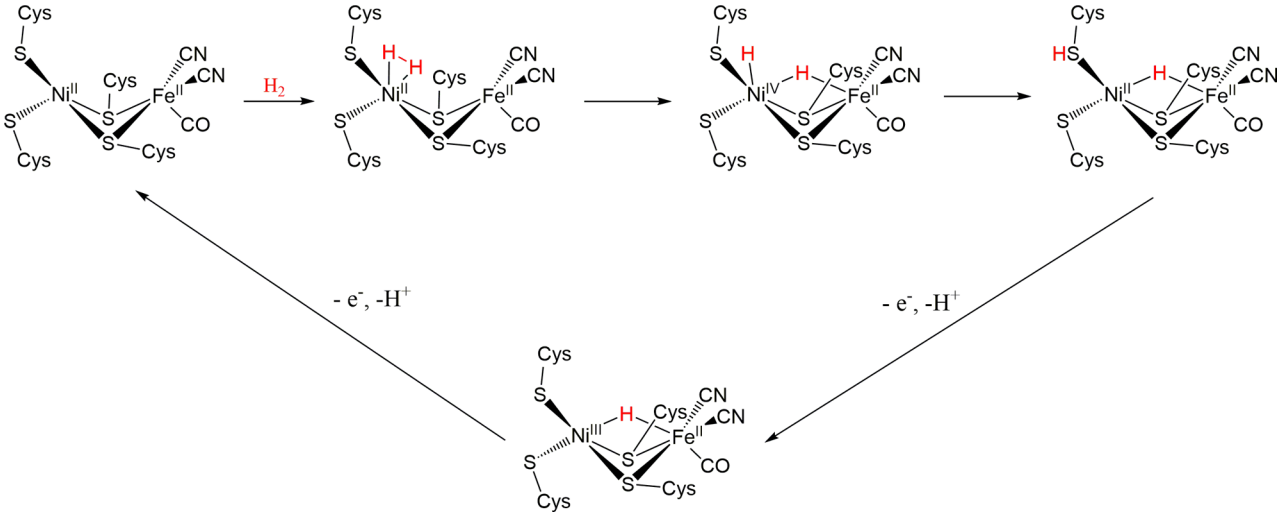

Another plausible mechanism might start with the H_2 cleavage on the Ni^{II} form but then proceed by a double proton and electron loss to form a Ni^0 species that can bind and cleave H_2 in an oxidative addition step. However, geometry optimization of such a Ni^0 form (hereafter labeled $^1\mathbf{0}_L$) obtained by two-electron reduction of $^1\mathbf{2}_L$ yields to a significant reorganization of the active site, with the S atom of Cys558 moving at a distance of about 3.2 Å from Ni and one CN^- ligand migrating to a semibridged position between the two metal atoms. In addition, binding of H_2 to Ni yields to a species ($^1\mathbf{0\text{-}Ni}_{H_2}$) featuring a full dissociation of the S atom of Cys555 and a significant rearrangement of the ligand configurations around the Ni atom, whereas binding of H_2 to Fe leads to an adduct ($^1\mathbf{0\text{-}Fe}_{H_2}$) which is more than 20 kcal mol^{-1} higher in energy than the reactants.

Finally, we also investigated the mechanism in which H_2 might bind to Ni^{II} in an enzyme form in which a hydride is already bridged between the two metal atoms. However, in this case, all attempts to obtain a H_2 adduct resulted in the dissociation of H_2. In addition, a plausible intermediate in which H_2 is heterolytically split in a terminal hydride on Ni and a proton on S_c evolves during geometry optimization to a structure in which the S atom of Cys61 moves at a distance of about 4 Å from Ni, leaving the metal atom in square pyramidal configuration with the bridging hydride and the terminal hydride occupying the apical and an equatorial position, respectively.

CONCLUSIONS

The disclosure of the stereoelectronic properties of the active site of [NiFe]-hydrogenases which are crucial for efficient H_2 binding and cleavage is important not only in the context of the efforts aimed at elucidating structure–function relationships in hydrogenases[15,65] but also for the rational design of novel bioinspired catalysts for H_2 oxidation.[66−71] To contribute to such an effort, we have used DFT to study the H_2 binding and activation properties of models of the active site of [NiFe]-hydrogenase, ranging from minimal (metal ions and first coordination sphere) to very large (metal cluster, first and second coordination sphere − 290 atoms). Results highlight that the spin state and the coordination geometry of the Ni ion are two crucial factors that tune the energetics and regiochemistry of H_2 binding to the NiFe metal cluster. In particular, (a) H_2 binding is energetically favored only when the NiFe metal cluster is in a low spin state and the Ni cysteine ligands have a distorted seesaw coordination geometry, as observed in the crystallographic structures of [NiFe]-hydrogenases. In addition, (b) when the Ni coordination sphere has such peculiar stereoelectronic features, H_2 binding is regiospecific and takes place exclusively at the Ni center. Two low activation energy pathways are possible after H_2 binding to the Ni^{II} ion: direct heterolytic cleavage of H_2 mediated by the sulfur atom of one of the terminally coordinated cysteine residues or oxidative addition of H_2 followed by proton transfer to the sulfur atom of one of the terminally coordinated cysteines. The latter reaction pathway is almost barrierless, indicating that H_2 cleavage can occur very quickly leading to the putative Ni-R form (Scheme 6).

The oxidative addition pathway also reveals that a transient (formal) Ni^{IV} species could be formed in the catalytic cycle of [NiFe]-hydrogenases. Notably, the product of H_2 cleavage formed according to an oxidative addition step followed by proton transfer to the S atom is indistinguishable from that obtained from direct heterolytic cleavage, and therefore in full agreement with experimental observations indicating heterolytic cleavage of H_2 in the active site of [NiFe]-hydrogenases.[16] More importantly, our results show that activation and cleavage of H_2 is strongly affected by the geometry of the ligands coordinated to the Ni atom, which must have a distorted seesaw arrangement (S_b–Ni–S_a < 135°; S_c–Ni–S_d > 160°) for efficient catalysis.

The formal transient formation of a Ni^{IV} dihydride species into the enzyme active site was never proposed before, but it is not without precedent when considering the chemistry of Ni-containing synthetic catalysts. In fact, DuBois et al., which have characterized the reactivity of several nickel complexes containing proton relays,[72] reported the detailed experimental dissection of the mechanism for electrochemical H_2 oxidation catalyzed by $[Ni(dppp)(P^{Ph}2N^{Bz}2)](BF_4)_2$, where $P^{Ph}2N^{Bz}2$ is 1,5-dibenzyl-3,7-diphenyl-1,5-diaza-3,7-diphosphacyclooctane and dppp is 1,3-bis(diphenylphosphino)propane.[73] Similarly to our observations, DuBois et al. found that the initial H_2 addition step involves the formation of a transient dihydrogen

dx.doi.org/10.1021/ja408511y | J. Am. Chem. Soc. 2014, 136, 1803−1814

complex, which then undergoes a rate determining H−H bond cleavage to form the corresponding Ni^{IV} dihydride complex, for which spectroscopic evidence was obtained. Then, the dihydride species evolves according to a reaction step in which one of the two hydrogen atoms coordinated to Ni is transferred as a proton to the N atom of the cyclic ligand. Notably, in the computed structure of the transient dihydrogen complex $H_2[Ni(dppp)(P^{Ph}2N^{Bz}2)]^{2+}$, the phosphine ligands do not remain in a slightly distorted square planar configuration (as observed in the reactant $[Ni(dppp)(P^{Ph}2N^{Bz}2)]^{2+}$) but assume an arrangement, similar to the seesaw geometry observed in the enzyme.

The observation that a seesaw Ni coordination geometry is a key feature for efficient H_2 binding and activation can be usefully discussed also in the light of other previous results that showed how H_2 binding and activation on Ni-containing functional models of hydrogenases is often concomitant with a drastic structural rearrangement of the metal coordination geometry. In particular, it was previously reported that H_2 binding and cleavage on [Ni(NHP*n*Pr$_3$)("S3")] (where S3 = bis(2-sulfanylphenyl)sulfide) is concomitant with the rearrangement of the Ni coordination environment from a square planar to a flattened tetrahedral geometry.[74] However, in the case of [Ni(NHP*n*Pre$_3$)("S3")], it was found that such a structural rearrangement is energetically very disfavored and this is the main cause of its poor catalytic properties. Our results show that such rearrangement does not take place in the enzyme, because in the four-coordinated low spin Ni species corresponding to the Ni-SI_a enzyme form, due to the stereoelectronic properties of the metal cluster environment, the Ni coordination sphere already has a distorted seesaw geometry, and not the classical square planar geometry that would be expected for simpler low spin Ni(II) coordination compounds.

From an electronic structure perspective, our results complement the observations made by DuBois et al., which highlighted how an increased driving force for H_2 addition is linked to the distortion of square planar Ni complexes, essentially because such a distortion leads to a decrease in the energy of the LUMO, which enhances the hydride acceptor ability of Ni^{II} complexes.[75,76] In addition, the observation that reaction energies for H_2 binding and cleavage in the minimal model $[(CH_3S)Ni]^{2-}$ are systematically less favorable than in bimetallic active site models underlines the noninnocent role of the $Fe(CO)(CN)_2$ moiety, and might encourage further studies aimed at understanding how the communication between the metals facilitates the electron transfer processes throughout the catalytic cycle.[77]

■ ASSOCIATED CONTENT

Supporting Information

Detailed information of the computational models, energies, and Cartesian coordinates of selected species investigated. This material is available free of charge via the Internet at http://pubs.acs.org.

■ AUTHOR INFORMATION

Corresponding Authors

maurizio.bruschi@unimib.it
luca.degioia@unimib.it

Notes

The authors declare no competing financial interest.

■ REFERENCES

(1) Wang, M.; Chen, L.; Sun, L. *Energy Environ. Sci.* **2012**, *5*, 6763−6778.
(2) Vignais, P. M.; Billoud, B. *Chem. Rev.* **2007**, *107*, 4206−4272.
(3) Parkin, A.; Sargent, F. *Curr. Opin. Chem. Biol.* **2012**, *16*, 26−34.
(4) Hexter, S. V.; Grey, F.; Happe, T.; Climent, V.; Armstrong, F. A. *Proc. Natl. Acad. Sci. U.S.A.* **2012**, *109*, 11516−11521.
(5) Abou Hamdan, A.; Dementin, S.; Liebgott, P.-P.; Gutierrez-Sanz, O.; Richaud, P.; De Lacey, A. L.; Roussett, M.; Bertrand, P.; Cournac, L.; Leger, C. *J. Am. Chem. Soc.* **2012**, *134*, 8368−8371.
(6) Tard, C.; Pickett, C. J. *Chem. Rev.* **2009**, *109*, 2245−2274.
(7) Mealli, C.; Rauchfuss, T. B. *Angew. Chem., Int. Ed.* **2007**, *46*, 8942−8944.
(8) Georgakaki, I. P.; Thomson, L. M.; Lyon, E. J.; Hall, M. B.; Darensbourg, M. Y. *Coord. Chem. Rev.* **2003**, *238*, 255−266.
(9) Volbeda, A.; Charon, M.; Piras, C.; Hatchikian, E.; Frey, M.; Fontecilla-Camps, J. *Nature* **1995**, *373*, 580−587.
(10) Volbeda, A.; Garcin, E.; Piras, C.; deLacey, A. L.; Fernandez, V. M.; Hatchikian, E. C.; Frey, M.; Fontecilla-Camps, J. C. *J. Am. Chem. Soc.* **1996**, *118*, 12989−12996.
(11) Happe, R. P.; Roseboom, W.; Pierik, A. J.; Albracht, S. P. J.; Bagley, K. A. *Nature* **1997**, *385*, 126−126.
(12) Pierik, A. J.; Roseboom, W.; Happe, R. P.; Bagley, K. A.; Albracht, S. P. J. *J. Biol. Chem.* **1999**, *274*, 3331−3337.
(13) Higuchi, Y.; Ogata, H.; Miki, K.; Yasuoka, N.; Yagi, T. *Structure* **1999**, *7*, 549−556.
(14) Volbeda, A.; Martin, L.; Cavazza, C.; Matho, M.; Faber, B. W.; Roseboom, W.; Albracht, S. P. J.; Garcin, E.; Rousset, M.; Fontecilla-Camps, J. C. *J. Biol. Inorg. Chem.* **2005**, *10*, 239−249.
(15) Fontecilla-Camps, J. C.; Volbeda, A.; Cavazza, C.; Nicolet, Y. *Chem. Rev.* **2007**, *107*, 4273−4303.
(16) Pandelia, M.-E.; Ogata, H.; Lubitz, W. *ChemPhysChem* **2010**, *11*, 1127−1140.
(17) Siegbahn, P. E. M.; Tye, J. W.; Hall, M. B. *Chem. Rev.* **2007**, *107*, 4414.
(18) Ogata, H.; Lubitz, W.; Higuchi, Y. *Dalton Trans.* **2009**, 7577−7587.
(19) De Lacey, A. L.; Pardo, A.; Fernandez, V. M.; Dementin, S.; Adryanczyk-Perrier, G.; Hatchikian, E. C.; Rousset, M. *J. Biol. Inorg. Chem.* **2004**, *9*, 636−642.
(20) De Lacey Antonio, L.; Fernandez, V. M.; Rousset, M.; Cammack, R. *Chem. Rev.* **2007**, *107*, 4304−4330.
(21) Kraemer, T.; Kampa, M.; Lubitz, W.; van Gastel, M.; Neese, F. *ChemBioChem* **2013**, *14*, 1898−1905.
(22) Niu, S.; Hall, M. B. *Inorg. Chem.* **2001**, *40*, 6201−6203.
(23) Montet, Y.; Amara, P.; Volbeda, A.; Vernede, X.; Hatchikian, E. C.; Field, M. J.; Frey, M.; Fontecilla-Camps, J. C. *Nat. Struct. Biol.* **1997**, *4*, 523−526.
(24) Wu, H.; Hall, M. B. *C. R. Chim.* **2008**, *11*, 790−804.
(25) Stein, M.; Lubitz, W. *J. Inorg. Biochem.* **2004**, *98*, 862−877.
(26) Lill, S. O. N.; Siegbahn, P. E. M. *Biochemistry* **2009**, *48*, 1056−1066.
(27) Amara, P.; Volbeda, A.; Fontecilla-Camps, J. C.; Field, M. J. *J. Am. Chem. Soc.* **1999**, *121*, 4468−4477.
(28) Dole, F.; Fournel, A.; Magro, V.; Hatchikian, E. C.; Bertrand, P.; Guigliarelli, B. *Biochemistry* **1997**, *36*, 7847−7854.
(29) Wang, C.; Franco, R.; Moura, J.; Moura, I.; Day, E. *J. Biol. Chem.* **1992**, *267*, 7378−7380.
(30) Kowal, A.; Zambrano, I.; Moura, I.; Moura, J.; Legall, J.; Johnson, M. *Inorg. Chem.* **1988**, *27*, 1162−1166.
(31) Wang, H. X.; Ralston, C. Y.; Patil, D. S.; Jones, R. M.; Gu, W.; Verhagen, M.; Adams, M.; Ge, P.; Riordan, C.; Marganian, C. A.; Mascharak, P.; Kovacs, J.; Miller, C. G.; Collins, T. J.; Brooker, S.; Croucher, P. D.; Wang, K.; Stiefel, E. I.; Cramer, S. P. *J. Am. Chem. Soc.* **2000**, *122*, 10544−10552.
(32) Bruschi, M.; De Gioia, L.; Zampella, G.; Reiher, M.; Fantucci, P.; Stein, M. *J. Biol. Inorg. Chem.* **2004**, *9*, 873−884.
(33) Reiher, M.; Salomon, O.; Hess, B. A. *Theor. Chem. Acc.* **2001**, *107*, 48−55.

(34) Ogata, H.; Kellers, P.; Lubitz, W. *J. Mol. Biol.* **2010**, *402*, 428−444.
(35) Siegbahn, P. E. M.; Himo, F. *J. Biol. Inorg. Chem.* **2009**, *14*, 643−651.
(36) Siegbahn, P. E. M.; Himo, F. *Rev. Comput. Mol. Sci.* **2011**, *1*, 323−336.
(37) Alberto, M. E.; Marino, T.; Russo, N.; Sicilia, E.; Toscano, M. *Phys. Chem. Chem. Phys.* **2012**, *14*, 14943−14953.
(38) Kampa, M.; Lubitz, W.; van Gastel, M.; Neese, F. *J. Biol. Inorg. Chem.* **2012**, *17*, 1269−1281.
(39) Dementin, S.; Burlat, B.; De Lacey, A. L.; Pardo, A.; Adryanczyk-Perrier, G.; Guigliarelli, B.; Fernandez, V. M.; Rousset, M. *J. Biol. Chem.* **2004**, *279*, 10508−10513.
(40) Teixeira, V. H.; Soares, C. M.; Baptista, A. M. *Proteins* **2008**, *70*, 1010−1022.
(41) Galvan, I. F.; Volbeda, A.; Fontecilla-Camps, J. C.; Field, M. J. *Proteins* **2008**, *73*, 195−203.
(42) Saggu, M.; Ludwig, M.; Friedrich, B.; Hildebrandt, P.; Bittl, R.; Lendzian, F.; Lenz, O.; Zebger, I. *ChemPhysChem* **2010**, *11*, 1215−1224.
(43) Ludwig, M.; Cracknell, J. A.; Vincent, K. A.; Armstrong, F. A.; Lenz, O. *J. Biol. Chem.* **2009**, *284*, 465−477.
(44) Ahlrichs, R.; Bar, M.; Haser, M.; Horn, H.; Kolmel, C. *Chem. Phys. Lett.* **1989**, *162*, 165−169.
(45) Becke, A. *Phys. Rev. A* **1988**, *38*, 3098−3100.
(46) Perdew, J. *Phys. Rev. B* **1986**, *33*, 8822−8824.
(47) Eichkorn, K.; Treutler, O.; Ohm, H.; Haser, M.; Ahlrichs, R. *Chem. Phys. Lett.* **1995**, *240*, 283−289.
(48) Schafer, A.; Huber, C.; Ahlrichs, R. *J. Chem. Phys.* **1994**, *100*, 5829−5835.
(49) Schafer, A.; Horn, H.; Ahlrichs, R. *J. Chem. Phys.* **1992**, *97*, 2571−2577.
(50) Klamt, A. *J. Phys. Chem.* **1995**, *99*, 2224−2235.
(51) Klamt, A.; Schuurmann, G. *J. Chem. Soc., Perkin Trans. 2* **1993**, 799−805.
(52) Grimme, S.; Antony, J.; Ehrlich, S.; Krieg, H. *J. Chem. Phys.* **2010**, *132*, 154104.
(53) Grimme, S. *J. Comput. Chem.* **2006**, *27*, 1787−1799.
(54) Grimme, S. *J. Comput. Chem.* **2004**, *25*, 1463−1473.
(55) Ahlrichs, R.; Bar, M.; Haser, M.; Horn, H.; Kolmel, C. *Chem. Phys. Lett.* **1989**, *162*, 165−169.
(56) Zhao, Y.; Truhlar, D. G. *J. Chem. Phys.* **2006**, *125*, No. 194101.
(57) Frisch, M. J.; Trucks, G. W.; Schlegel, H. B.; Scuseria, G. E.; Robb, M. A.; Cheeseman, J. R.; Scalmani, G.; Barone, V.; Mennucci, B.; Petersson, G. A.; Nakatsuji, H.; Caricato, M.; Li, X.; Hratchian, H. P.; Izmaylov, A. F.; Bloino, J.; Zheng, G.; Sonnenberg, J. L.; Hada, M.; Ehara, M.; Toyota, K.; Fukuda, R.; Hasegawa, J.; Ishida, M.; Nakajima, T.; Honda, Y.; Kitao, O.; Nakai, H.; Vreven, T.; Montgomery, J. A., Jr.; Peralta, J. E.; Ogliaro, F.; Bearpark, M.; Heyd, J. J.; Brothers, E.; Kudin, K. N.; Staroverov, V. N.; Kobayashi, R.; Normand, J.; Raghavachari, K.; Rendell, A.; Burant, J. C.; Iyengar, S. S.; Tomasi, J.; Cossi, M.; Rega, N.; Millam, N. J.; Klene, M.; Knox, J. E.; Cross, J. B.; Bakken, V.; Adamo, C.; Jaramillo, J.; Gomperts, R.; Stratmann, R. E.; Yazyev, O.; Austin, A. J.; Cammi, R.; Pomelli, C.; Ochterski, J. W.; Martin, R. L.; Morokuma, K.; Zakrzewski, V. G.; Voth, G. A.; Salvador, P.; Dannenberg, J. J.; Dapprich, S.; Daniels, A. D.; Farkas, Ö.; Foresman, J. B.; Ortiz, J. V.; Cioslowski, J.; Fox, D. J. *Gaussian 09*, revision D.01; Gaussian, Inc.: Wallingford, CT, 2009.
(58) Helgaker, T. *Chem. Phys. Lett.* **1991**, *182*, 503−510.
(59) Bruschi, M.; Zampella, G.; Fantucci, P.; De Gioia, L. *Coord. Chem. Rev.* **2005**, *249*, 1620−1640.
(60) Fontecilla-Camps, J. C.; Amara, P.; Cavazza, C.; Nicolet, Y.; Volbeda, A. *Nature* **2009**, *460*, 814−822.
(61) Fritsch, J.; Scheerer, P.; Frielingsdorf, S.; Kroschinsky, S.; Friedrich, B.; Lenz, O.; Spahn, C. M. T. *Nature* **2011**, *479*, 249−U134.
(62) Niu, S. Q.; Thomson, L. M.; Hall, M. B. *J. Am. Chem. Soc.* **1999**, *121*, 4000−4007.
(63) Keith, J. M.; Hall, M. B. *Inorg. Chem.* **2010**, *49*, 6378−6380.
(64) Pardo, A.; De Lacey, A. L.; Fernandez, V. M.; Fan, H. J.; Fan, Y. B.; Hall, M. B. *J. Biol. Inorg. Chem.* **2006**, *11*, 286−306.
(65) Stiebritz, M. T.; Reiher, M. *Chem. Sci.* **2012**, *3*, 1739−1751.
(66) Ogo, S.; Ichikawa, K.; Kishima, T.; Matsumoto, T.; Nakai, H.; Kusaka, K.; Ohhara, T. *Science* **2013**, *339*, 682−684.
(67) Ogo, S.; Kabe, R.; Uehara, K.; Kure, B.; Nishimura, T.; Menon, S. C.; Harada, R.; Fukuzumi, S.; Higuchi, Y.; Ohhara, T.; Tamada, T.; Kuroki, R. *Science* **2007**, *316*, 585−587.
(68) Carroll, M. E.; Barton, B. E.; Gray, D. L.; Mack, A. E.; Rauchfuss, T. B. *Inorg. Chem.* **2011**, *50*, 9554−9563.
(69) Schilter, D.; Nilges, M. J.; Chakrabarti, M.; Lindahl, P. A.; Rauchfuss, T. B.; Stein, M. *Inorg. Chem.* **2012**, *51*, 2338−2348.
(70) Fourmond, V.; Canaguier, S.; Golly, B.; Field, M. J.; Fontecave, M.; Artero, V. *Energy Environ. Sci.* **2011**, *4*, 2417−2427.
(71) Canaguier, S.; Field, M.; Oudart, Y.; Pécaut, J.; Fontecave, M.; Artero, V. *Chem. Commun.* **2010**, *46*, 5876−5878.
(72) Small, Y. A.; DuBois, D. L.; Fujita, E.; Muckerman, J. T. *Energy Environ. Sci.* **2011**, *4*, 3008−3020.
(73) Yang, J. Y.; Bullock, R. M.; Shaw, W. J.; Twamley, B.; Fraze, K.; DuBois, M. R.; DuBois, D. L. *J. Am. Chem. Soc.* **2009**, *131*, 5935−5945.
(74) Zampella, G.; Bruschi, M.; Fantucci, P.; De Gioia, L. *J. Am. Chem. Soc.* **2005**, *127*, 13180−13189.
(75) DuBois, D. L.; Blake, D. M.; Miedaner, A.; Curtis, C. J.; DuBois, M. R.; Franz, J. A.; Linehan, J. C. *Organometallics* **2006**, *25*, 4414−4419.
(76) Raebiger, J. W.; Miedaner, A.; Curtis, C. J.; Miller, S. M.; Anderson, O. P.; DuBois, D. L. *J. Am. Chem. Soc.* **2004**, *126*, 5502−5514.
(77) Weber, K.; Krämer, T.; Shafaat, H. S.; Weyhermüller, T.; Bill, E.; van Gastel, M.; Neese, F.; Lubitz, W. *J. Am. Chem. Soc.* **2012**, *134*, 20745−20755.